



## Turbulence model form errors in separated flows

Kerry S. Klemmer <sup>1,\*</sup>, Wen Wu <sup>2</sup> and Michael E. Mueller<sup>1</sup><sup>1</sup>*Department of Mechanical and Aerospace Engineering, Princeton University,  
Princeton, New Jersey 08544, USA*<sup>2</sup>*Department of Mechanical Engineering, University of Mississippi, Oxford, Mississippi 38677, USA*

(Received 18 June 2022; accepted 20 January 2023; published 15 February 2023)

In turbulence modeling, model form errors are introduced in the prediction of the Reynolds stresses through the Boussinesq hypothesis and other modeling choices, such as the specific form of the eddy viscosity. These linear eddy viscosity models have known points of failure in flows that feature significant complexity, such as separated flows. In this work, an implied models approach is used to better understand the sources and dynamics of model form error in separated flows through *a priori* analysis, focusing on the Boussinesq hypothesis using exact inputs for determining the eddy viscosity. In the implied models approach, a transport equation is derived for the model error through the transport equation implied by the model for the quantity of interest; that is, the Reynolds stresses in this work. A boundary layer over a flat plate with a statistically stationary separation bubble is analyzed and shown to have two error modes corresponding to the qualitative behavior of turbulent wall-bounded and turbulent free-shear model form errors. The wall-bounded mode is observed sufficiently upstream of the separation bubble, and the free-shear mode is observed near and within the separation bubble, with a superposition of these two modes observed in the intermediate regions. These results indicate on the one hand a complex picture of model error that changes through the flow but on the other hand a simple picture of model error that comprises elements of canonical flows. Therefore, calibration of turbulence models against simpler canonical flows can capture the main modes of model failure in more complex flows.

DOI: [10.1103/PhysRevFluids.8.024606](https://doi.org/10.1103/PhysRevFluids.8.024606)

### I. INTRODUCTION

Reynolds-averaged Navier-Stokes (RANS) models are popular tools due to their relatively inexpensive computational cost compared with large eddy simulation (LES) and direct numerical simulation (DNS). The physical assumptions that give rise to these models are well suited to certain flows, specifically flows that are in a state of quasi-equilibrium. In practice, this designation can only be applied to fairly simple flows that do not have features that violate the tenuous nature of quasi-equilibrium turbulent flow. Transgressive features include, but are not limited to, sudden changes in mean strain rate, curved surfaces, rotation, and three-dimensionality [1]. Due to the limitations of quasi-equilibrium turbulence, in theory, the simplest, complete RANS models, such as the two equation  $k$ - $\varepsilon$  and  $k$ - $\omega$  models, only provide valid predictions for flows with slowly varying properties, such as homogeneous or free-shear flows.

In practice, however, two equation RANS models are also able to provide predictions that match well with high fidelity data for canonical flows that have sharp gradients and thus properties that are not slowly varying (e.g., wall-bounded flows), although this has been shown to be the result of

---

\*kklemmer@princeton.edu

fortuitous error cancellation [2]. In many cases, these models require flow specific corrections, such as wall functions [3], cross-diffusion terms for free shear flows [4], or stress limiters applied to the eddy viscosity for shock waves in compressible flows [5]. While not necessarily a disadvantage, the need for such corrections poses a challenge for the generalizability of RANS models, requiring that knowledge of key physical features of a flow is necessarily understood prior to simulation. This is particularly challenging for complex flows in which *a priori* knowledge is often unavailable or unattainable.

One particular class of complex flows that challenge the predictive capabilities of RANS models is flows with separation, characterized by boundary layer detachment and flow reversal near a solid surface. Standard linear eddy viscosity RANS models often fail to accurately predict the characteristics of separation in a given flow, such as the reattachment point in a backward-facing step [6], location of separation and reattachment points in a separation bubble [1], and the size of the recirculation zone in flow past both square and circular cylinders [7]. To rectify this, corrections have been made to account for discrepancies between model predictions and experimental or numerical data. For example, in Knopp *et al.* [8], a wall function was employed with the Spalart-Allmaras and  $k-\omega$  models for compressible flow and was shown to improve the prediction of the reattachment point in flow over an airfoil. An alternative approach has been to use a hybrid RANS approach that also incorporates a higher fidelity model, such as a LES or a detached eddy simulation (DES) [9]. The drawback of a hybrid approach is that the higher-fidelity model necessitates an increased computational cost.

As the models continue to adapt to be able to better predict separated flow features, uncertainty quantification is a necessary tool for understanding the reliability and fidelity of the model predictions. Multiple works have quantified uncertainty in separated flows, looking at a range of RANS models and both model-form [10–12] and parameter [13,14] uncertainties. The works focused on parametric uncertainty have explored the sensitivity of the models to the values of the parameters in separated flows [13], and have also explored more cost-effective methods for quantifying this kind of uncertainty, such as latin hypercube sampling [14]. In general, parametric uncertainty, while important for understanding a model’s sensitivity, does not address the underlying physical assumptions in the models. Parameter uncertainty quantification can be used to more accurately tune model parameters but cannot help to improve the physical accuracy of the model, where physical accuracy is lacking.

In contrast, model-form uncertainty quantification is able to address the physical deficiencies in these models. In Górlé *et al.* [15], a marker function technique was used based on deviation from parallel shear flow in two flows with regions of separation. This method, while successful in identifying regions of linear eddy viscosity model failure, only focused on one particular assumption present in these models. In Górlé *et al.* [11], Iaccarino *et al.* [10], and Thompson *et al.* [12], the approach developed by Emory *et al.* [16] was used and adapted in studying a separated flow case. In this approach, the anisotropic stress tensor is decomposed into its eigenvalues and eigenvectors, and perturbations are introduced in order to provide error bounds on the quantity of interest. In Górlé *et al.* [11], uncertainty in flow over a wavy wall was analyzed. The production of turbulent kinetic energy was found to have the largest effect on the prediction of the Reynolds stresses, so perturbations to the turbulent kinetic energy were introduced via this term and also the eigenvalues of the anisotropic Reynolds stress tensor. In contrast, in both Refs. [10,12], the eigenvector perturbations were studied, citing misalignment between the mean strain rate and anisotropic Reynolds stress tensor as one of the major sources of model error in linear eddy viscosity RANS models. For various separated-flow cases (flow over a backward facing step and flow in an axisymmetric diffuser), with the introduction of the eigenvector perturbations, the models were able to provide better predictions compared with solely using eigenvalue perturbations. These works highlight the shortcomings of these models for separated flows and provide insight into the response of the models to various perturbations. However, these approaches utilize a given model structure to quantify model error, rather than identify the physics not captured by the model. Therefore, physics-based uncertainty

quantification analysis of separated flows that explore the sources and structure of the model error serve to enhance general understanding of RANS model limitations.

In this work, an *implied models* approach—a physics-based uncertainty quantification methodology developed by Klemmer and Mueller [2]—is used to analyze model error first in a turbulent planar jet to understand the model error in a canonical free-shear flow, building upon previous work on turbulent channel flow to understand the model error in a canonical wall-bounded flow [2]. Then, the implied models approach is used to understand the model error in a turbulent boundary layer over a flat plate with a statistically stationary separation bubble to understand the physical mechanisms responsible for model failure. The general approach is outlined in Sec. II; the planar jet results are presented in Sec. III; the separation bubble results are presented in Sec. IV; and the implications of these results are discussed in Sec. V.

## II. IMPLIED MODELS APPROACH

In the implied models approach [2], the model error  $e$  is defined as the difference between a true physical quantity  $\mathcal{R}$  and the modeled quantity  $\mathcal{M}$ :

$$e = \mathcal{R} - \mathcal{M}. \quad (1)$$

The quantity  $\mathcal{R}$  is assumed to have an exact transport equation, and it is also assumed that an analogous transport equation can be derived for the modeled quantity  $\mathcal{M}$ . The transport equation for the model error can then be derived by taking the difference between these two transport equations:

$$\frac{De}{Dt} = \frac{D\mathcal{R}}{Dt} - \frac{D\mathcal{M}}{Dt}. \quad (2)$$

In turbulence, a transport equation can be derived for almost any physical quantity, a fact exploited in this method. In the present work, the anisotropic Reynolds stress tensor  $a_{ij}$  is taken to be the true physical quantity:

$$\mathcal{R}_{ij} = a_{ij} = \overline{u'_i u'_j} - \frac{2}{3} k \delta_{ij}, \quad (3)$$

where  $\overline{u'_i u'_j}$  is the Reynolds stress tensor and  $k = \frac{1}{2} \overline{u'_i u'_i}$  is the turbulent kinetic energy. The model used in this work for the anisotropic Reynolds stress tensor is the Boussinesq eddy viscosity model:

$$\mathcal{M}_{ij} = -2\nu_T S_{ij}, \quad (4)$$

where  $\nu_T$  is the eddy viscosity and  $S_{ij} = \frac{1}{2} (\frac{\partial U_i}{\partial x_j} + \frac{\partial U_j}{\partial x_i})$  is the mean strain rate tensor. The model error and its transport equation are then found by substituting Eqs. (3) and (4) into Eqs. (1) and (2), yielding

$$e_{ij} = a_{ij} + 2\nu_T S_{ij} \quad (5)$$

and

$$\frac{\overline{D}e_{ij}}{Dt} = \frac{\overline{D}a_{ij}}{Dt} + 2\nu_T \frac{\overline{D}S_{ij}}{Dt} + 2S_{ij} \frac{\overline{D}\nu_T}{Dt}, \quad (6)$$

where  $\overline{D}/Dt$  is the mean Lagrangian derivative in which advection is by the mean velocity  $U_k$ . The transport equation for the model error  $e_{ij}$  is derived through the specification of the three transport equations in Eq. (6) for the anisotropic Reynolds stress tensor, the mean strain rate tensor, and the eddy viscosity. The transport equations for  $\nu_T$  depend on the choice of the model. There are many different choices for the eddy viscosity based on the variables chosen to represent  $\nu_T$  and also whether the transport equations for these variables are exactly derived or modeled. In this work, the standard  $k$ - $\varepsilon$  and  $k$ - $\omega$  [1] models are explored, and the exact transport equations for  $k$ ,  $\varepsilon$ , and  $\omega$  are used and evaluated with high-fidelity data. Note that using the exact transport equations for these

TABLE I. Simulation parameters for the turbulent planar jet.  $L_x$ ,  $L_y$ ,  $L_z$  are the dimensions in the streamwise, cross-stream, and spanwise directions;  $N_x$ ,  $N_y$ , and  $N_z$  are the number of grid points in the streamwise, cross-stream, and spanwise directions; and  $\Delta x/H$ ,  $\Delta z/H$ , and  $\Delta y_c/H$  are the grid spacings in the streamwise, spanwise, and cross-stream (at the centerline) directions normalized by the jet height  $H$  at the inlet.

$Re_H$	$L_x$	$L_y$	$L_z$	$N_x \times N_y \times N_z$	$\Delta x/H$	$\Delta z/H$	$\Delta y_c/H$
5000	$25H$	$24H$	$3H$	$768 \times 576 \times 256$	0.03211	0.01176	0.00163

quantities results in equivalent formulations for these two models, such that only one analysis is presented for both model forms.

Additional *a priori* and *a posteriori* analyses using the modeled transport equations for  $k$ ,  $\varepsilon$ , and  $\omega$  were performed in Klemmer and Mueller [2] for a turbulent channel flow. The model equation *a priori* analysis was shown to be overwhelmed by large errors that were introduced due to the physical inadequacy of the model transport equations relative to their exact counterparts. The *a posteriori* analysis in contrast did not exhibit these large errors and is instead illustrative of the degree of error cancellation between the Boussinesq model and the modeled transport equations for  $k$ ,  $\varepsilon$ , and  $\omega$ . However, the challenge in the present work is that the  $k$ - $\varepsilon$  and  $k$ - $\omega$  models are not known to be appropriate for flows with separation and reattachment. As such, prediction errors generated upstream would propagate downstream and accumulate, making it difficult to parse the sources of model error in a given region of the flow. In the present work, these additional analyses are not undertaken since the main objective of this paper is to study the deficiencies of the linear eddy viscosity model, which would be obfuscated by the sources of error mentioned above.

With all of these transport equations, a transport equation for the model error is derived by substituting the transport equations for  $a_{ij}$ ,  $S_{ij}$ , and the chosen equations for the transport of  $v_T$  into Eq. (6). The error transport equation, in compact form, is given by

$$\frac{\overline{D}e_{ij}}{Dt} = \mathcal{P}_{e_{ij}} + \mathcal{T}_{e_{ij}} + \mathcal{R}_{e_{ij}} - \varepsilon_{e_{ij}}, \quad (7)$$

where  $\mathcal{P}_{e_{ij}}$  represents production terms (nonviscous source),  $\mathcal{T}_{e_{ij}}$  represents transport terms (divergence of a flux),  $\mathcal{R}_{e_{ij}}$  represents redistribution terms (traceless contributions without a counterpart in the turbulent kinetic-energy transport equation), and  $\varepsilon_{e_{ij}}$  represents dissipation terms (viscous source).

The detailed derivation of the model error transport equation and the specification of Eq. (6) are presented in Klemmer and Mueller [2].

### III. TURBULENT PLANAR JET ANALYSIS

The implied models approach has been previously utilized to analyze the model error in a turbulent channel flow. In this work, a turbulent planar jet is first analyzed to understand the difference in the model error between these two canonical flows. A turbulent planar jet with  $Re_H = UH/\nu = 5000$ , where  $Re_H$  is the Reynolds number,  $U$  is the bulk velocity of the inflow, and  $H$  is the jet height, was simulated using NGA, which is a structured, finite difference solver [17, 18]. The computational details of the simulation can be found in Table I.  $L_x$ ,  $L_y$ , and  $L_z$  are the domain size in the streamwise, cross-stream, and spanwise directions, respectively, normalized by the jet height  $H$ .  $N_x$ ,  $N_y$ , and  $N_z$  are the number of grid points in the streamwise, cross-stream, and spanwise directions, respectively, resulting in the nondimensional uniform grid spacings  $\Delta x/H$  and  $\Delta z/H$  in the streamwise and spanwise directions, and the nondimensional nonuniform grid spacing  $\Delta y/H$  in the cross-stream direction. For the inflow, a channel profile was used that matched the bulk Reynolds number of the jet. At worst, there are a few locations where the ratio of the local grid spacing to the Kolmogorov length scale is up to a factor of  $\approx 5.5$ . However, additional limited

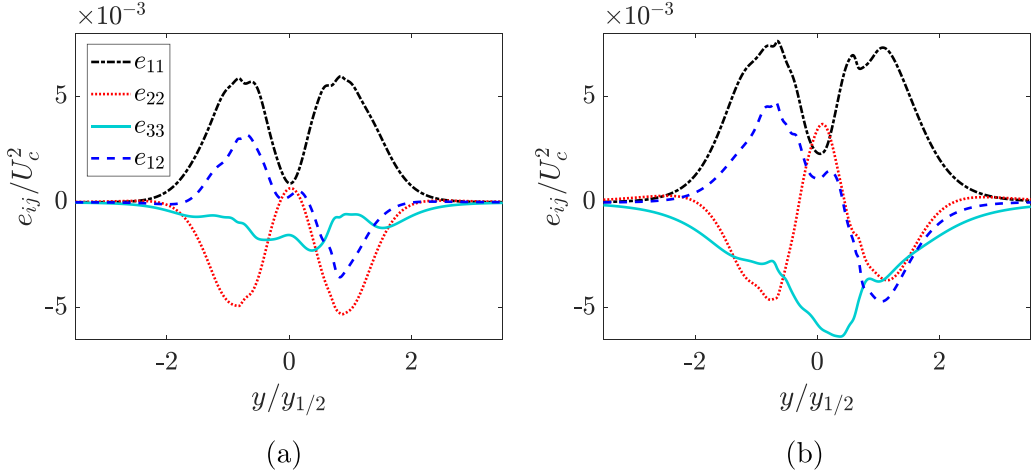


FIG. 1. Model error  $e_{ij}$  in the turbulent planar jet. (a)  $x/H = 5$  and (b)  $x/H = 10$ .

statistics were collected for a finer grid and indicated only very minor changes to the model error budgets that do not affect the qualitative behavior discussed in this work.

Cross-stream statistics in the planar jet are taken at two streamwise locations,  $x/H = 5$  and  $x/H = 10$ , and are normalized by the local mean centerline velocity  $U_c$  and the jet half-width  $y_{1/2}$ . Due to noise in the statistics, a moving average with a Gaussian filter in MATLAB (the `smoothdata` function [19]) was used to smooth the model error and model error budgets. In moving downstream, there is a slight increase in the magnitude of the model error, particularly in the  $e_{11}$  and  $e_{33}$  model error components, but overall the model errors at the two streamwise locations are qualitatively similar [see Figs. 1(a) and 1(b)]. Analysis of the model error budgets at  $x/H = 5$  [Figs. 2(a)–2(c)] and at  $x/H = 10$  [Figs. 2(d)–2(f)] points to a similar behavior. Figure 2 shows the model error production, dissipation, and redistribution at  $x/H = 5$  and  $x/H = 10$ . The dominant component of the model error production is the streamwise error term  $\mathcal{P}_{e_{11}}$ ; however, all four components are roughly of the same order. The terms that contribute most to the model error production for each component are

$$\mathcal{P}_{e_{11}} \approx 2v_T \frac{\partial U_1}{\partial x_2} \frac{\partial U_1}{\partial x_2} - 2e_{12} \frac{\partial U_1}{\partial x_2} + \frac{2}{3}(e_{k\ell} - 2v_T S_{k\ell}) \frac{\partial U_k}{\partial x_\ell}, \quad (8)$$

$$\mathcal{P}_{e_{22}} \approx \mathcal{P}_{e_{33}} \approx \frac{2}{3}(e_{k\ell} - 2v_T S_{k\ell}) \frac{\partial U_k}{\partial x_\ell}, \quad (9)$$

$$\mathcal{P}_{e_{12}} \approx -e_{22} \frac{\partial U_1}{\partial x_2} + 2v_T \frac{\partial U_1}{\partial x_2} \frac{\partial U_2}{\partial x_2} - 2 \frac{\partial v_T}{\partial x_2} \frac{\partial v_T S_{12}}{\partial x_2} + \frac{\partial v_T}{\partial x_2} \frac{\partial e_{12}}{\partial x_2}. \quad (10)$$

All the terms in Eqs. (8) and (9) and the first two terms in Eq. (10) arise from the discrepancy between the production predicted by the models and exact production, indicating that these errors come from the misalignment of the anisotropic Reynolds stress tensor and the mean strain rate tensor. While the relevant terms in the normal components of the model error production are the same as those found in turbulent channel flow [2], there are important differences. In particular, in the streamwise component in the planar jet,  $2v_T(\partial U_1/\partial x_2)(\partial U_1/\partial x_2)$  is roughly three times larger than  $2e_{12}\partial U_1/\partial x_2$ , while in the channel  $2v_T(\partial U_1/\partial x_2)(\partial U_1/\partial x_2)$  is roughly equivalent to  $2e_{12}\partial U_1/\partial x_2$ . In comparing these two terms, the important differences arise in the comparison of the shear component model error  $e_{12}$  with the shear component model  $v_T\partial U_1/\partial x_2$ . When the magnitude of  $e_{12}$  relative to the magnitude of  $v_T\partial U_1/\partial x_2$  is small, this indicates that the model performs relatively well compared with a case where the magnitude of  $e_{12}$  relative to the magnitude of

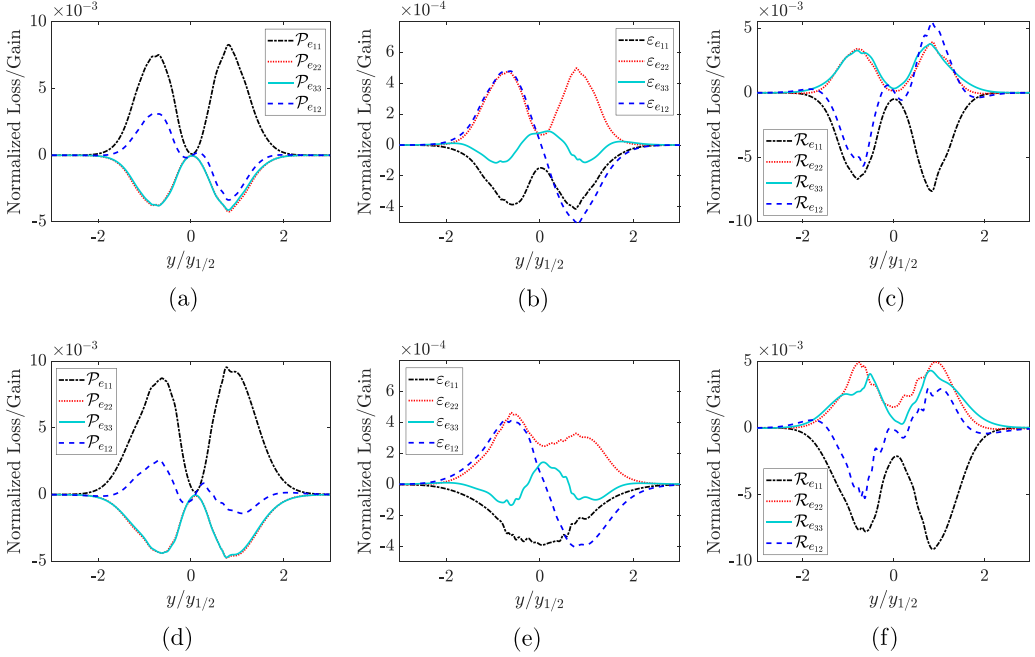


FIG. 2. Budgets for  $e_{ij}$  in the turbulent planar jet. (a)  $x/H = 5$ : Production, (b)  $x/H = 5$ : Dissipation, (c)  $x/H = 5$ : Redistribution, (d)  $x/H = 10$ : Production, (e)  $x/H = 10$ : Dissipation, and (f)  $x/H = 10$ : Redistribution.

$v_T \partial U_1 / \partial x_2$  is comparable or larger. Additionally, in the shear component of model error production, there is a minor (less than 15% of the largest term) additional misalignment term [the second term in Eq. (10)], which is not present in the channel due to the unidirectional nature of the flow. This illustrates the ways in which the two-dimensionality of the flow can contribute to the model error.

Another interesting difference is observed when studying the inhomogeneity terms that arise from wall-normal or cross-stream derivatives of the eddy viscosity. These terms are significant in the shear component and wall-normal component in the channel, and, while they are present in the shear and cross-stream components in the planar jet, they are not nearly as significant in terms of their relative magnitudes. In the wall-normal component in the channel, the model error production is also given by Eq. (9). Additionally, however, there are also large inhomogeneity terms given by

$$\frac{\partial v_T}{\partial x_2} \frac{\partial e_{22}}{\partial x_2} + \frac{4}{3} \frac{\partial v_T}{\partial x_2} \frac{\partial k}{\partial x_2}, \quad (11)$$

that are balanced by  $\frac{2}{\rho} (\partial v_T / \partial x_2) (\partial P / \partial x_2)$ , such that they do not contribute to the overall model error production in the wall-normal component. In the jet, these terms are also present and are balanced in the same way so that they do not contribute to the overall model error production in the cross-stream component. The differences in the inhomogeneity terms are seen in their relative magnitudes (similar to the discussion of the relevant terms in the streamwise model error production above). In the wall-normal model error production in the channel,  $(\partial v_T / \partial x_2) (\partial k / \partial x_2)$  and  $(\partial v_T / \partial x_2) (\partial e_{22} / \partial x_2)$  are both roughly an order of magnitude larger than  $\frac{2}{3} (e_{k\ell} - 2v_T S_{k\ell}) \partial U_k / \partial x_\ell$ . In the jet, these terms at their peak are only about 1/3 of the peak of the most dominant term  $\frac{2}{3} (e_{k\ell} - 2v_T S_{k\ell}) \partial U_k / \partial x_\ell$ . Similarly, in the channel shear component,  $2(\partial v_T / \partial x_2) (\partial v_T S_{12} / \partial x_2)$  and  $(\partial v_T / \partial x_2) (\partial e_{12} / \partial x_2)$  are comparable in magnitude to  $e_{22} \partial U_1 / \partial x_2$ , while in the jet the peaks of the inhomogeneity terms are roughly an order of magnitude smaller than the peak of the largest term  $e_{22} \partial U_1 / \partial x_2$ . This is due to the very steep gradients present in the vicinity of the walls in the channel (relative to those in the

planar jet or free-shear flows in general), which lead to rapid changes in the state of the turbulence in the near wall region.

The model error dissipation is roughly an order of magnitude smaller than the model error production and redistribution, which is another point of departure from the model error budgets in a turbulent channel [2]. This is due to the fact that, in free shear flows, the turbulence is relatively isotropic at the small scales [20,21], which means that the dissipation is well described by an isotropic model dissipation. Again, this is not true in the vicinity of a solid boundary. The isotropic nature of the small scales is also an important factor in the model error redistribution because, in the normal components, the dominant term is given by

$$\mathcal{R}_{e_{ij}} \approx -\frac{1}{\rho} \left\langle u'_i \frac{\partial p'}{\partial x_j} + u'_j \frac{\partial p'}{\partial x_i} \right\rangle + \frac{2}{3\rho} \frac{\partial u'_k p'}{\partial x_k} \delta_{ij}, \quad (12)$$

which is the pressure redistribution term. This indicates the importance of the pressure redistribution mechanism in the jet because this physical mechanism is the means through which the small scales achieve local isotropy. This “return to isotropy” has been theoretically outlined for inhomogeneous shear flows [22] and shown experimentally for a planar jet [23]. Additionally, this highlights the lack of redistributive mechanism in these simple RANS models, and their inability to capture nonlocal effects. In the streamwise and cross-stream components there is an additional, but minor, contribution from misalignment, specifically  $-4/3kS_{ij}$ . This misalignment term is also important in the shear component error redistribution, where the pressure redistribution also contributes, but to a lesser extent. The shear component redistribution is then given by

$$\mathcal{R}_{e_{12}} \approx -\frac{4}{3}kS_{12} - \frac{1}{\rho} \left\langle u'_1 \frac{\partial p'}{\partial x_2} + u'_2 \frac{\partial p'}{\partial x_1} \right\rangle. \quad (13)$$

This differs slightly from the turbulent channel analysis, in that pressure redistribution and misalignment contribute to the redistribution errors in each component (except for the spanwise component where misalignment is not relevant), with pressure redistribution dominating for the normal components and misalignment dominating for the shear component. This difference arises due to the two-dimensional nature of the planar jet flow in contrast to the channel. As a result, the normal components of the mean strain rate are no longer zero, so they contribute to the normal model error redistribution.

In the turbulent planar jet, the dominant sources of model error in the anisotropic Reynolds stresses are found to be misalignment of the anisotropic Reynolds stress tensor and mean strain rate tensor and the lack of redistribution mechanisms in the models. In contrast to the turbulent channel [2], there does not appear to be any overly dominant component, as there was with the shear component of the model error in the turbulent channel. Additionally, the small-scale isotropy in the planar jet (and generally in free shear flows) manifests in two ways. First, the model error dissipation was found to be an order of magnitude smaller than the model error production and redistribution, indicating that isotropic dissipation is a reasonable assumption for this flow. Second, the pressure redistribution term is shown to be an integral mechanism in this flow, and, although it is present in the normal component model error redistribution in the channel, the dominance of the shear component redistribution and the large model error dissipation indicates that shear misalignment and small-scale anisotropy play a much larger role in the model error in wall-bounded flows.

#### IV. SEPARATION BUBBLE ANALYSIS

The implied models approach is used to analyze a turbulent boundary layer over a flat plate with a separation bubble. This flow is used to highlight the shortcomings of the Boussinesq hypothesis and the  $k$ - $\varepsilon$  and the  $k$ - $\omega$  eddy viscosity models in flows with more complex strain, which are known points of failure for these models. In performing this analysis, the deficiencies in these models are better understood for these kinds of flow configurations, and novel insight is provided into the specific physics.

TABLE II. Simulation parameters for the statistically stationary separation bubble.  $L_x$ ,  $L_y$ , and  $L_z$  are the dimensions in the streamwise, wall-normal, and spanwise directions;  $N_x$ ,  $N_y$ , and  $N_z$  are the number of grid points in the streamwise, wall-normal, and spanwise directions; and  $\Delta x^+$ ,  $\Delta z^+$ , and  $\Delta y_{\min}^+$  are the grid spacing in the streamwise, spanwise, and wall-normal (at the wall) directions.

$Re_{\theta_0}$	$Re_{\tau_0}$	$L_x$	$L_y$	$L_z$	$N_x \times N_y \times N_z$	$\Delta x^+$	$\Delta z^+$	$\Delta y_{\min}^+$
2500	830	$570\theta_0$	$70\theta_0$	$54\theta_0$	$2560 \times 384 \times 384$	23	15	0.85

The data for the separation bubble test case come from Wu and Piomelli [24] and have been generated using wall-resolved LES, where the subfilter stresses are modeled by the integral length scale approximation (ILSA) model [25] in its local form [26]. The details of the simulation can be found in Table II, and Fig. 3 shows the mean streamwise velocity in the  $x$ - $y$  plane. The two Reynolds numbers shown are both based off of values taken at  $x = 0$ . Specifically,  $Re_{\theta_0} = U_0\theta_0/\nu$ , where the free stream velocity is  $U_0 = U_\infty(x = 0)$  and  $\theta_0$  is the momentum thickness at  $x = 0$ . These two quantities are used to normalize the data in all the subsequent figures, unless otherwise specified. The friction Reynolds number is given by  $Re_{\tau_0} = u_{\tau_0}\delta_0/\nu$ , where  $u_{\tau_0}$  is the friction velocity at  $x = 0$  and  $\delta_0$  is the boundary layer thickness at  $x = 0$ . The friction velocity and the viscous length scale  $\delta_v = \nu/u_\tau$  are the scales used for normalization when inner units are used.

The model error transport equation in this case is slightly modified due to the fact that the separation bubble utilizes data from LES. As a result, the viscosity  $\nu$  is taken to be the sum of the subfilter viscosity  $\nu_{SFS}$  and the kinematic viscosity  $\nu_0$ . This modified viscosity is now an instantaneous, spatially varying quantity and is decomposed in the Reynolds-averaging operation, such that  $\nu = \mathcal{V} + \nu'$ , where  $\mathcal{V}$  is the mean total viscosity and  $\nu'$  is the fluctuating total viscosity. The derivation of the model error transport equation for this case of incompressible flow with variable viscosity is given in Appendix. The additional terms that are present in the model error transport equation are only found to be significant in the model error dissipation. Additionally, it should be noted that, due to the nature of the data and noise in the statistics near and within the separation bubble, a moving average with a Gaussian filter in MATLAB (as in Sec. III) was used to smooth the model error and model error budgets for the streamwise locations downstream of  $x/\theta_0 = 0$ .

Figure 4 shows the model error  $e_{ij}$  at four streamwise locations in the flow: far upstream of the separation bubble in the zero pressure gradient region [Fig. 4(a)], roughly at the mean separation point [Fig. 4(b)], inside the separation bubble [Fig. 4(c)], and downstream of the reattachment point [Fig. 4(d)]. The nature of the model error clearly changes moving downstream, behaving more like a fully wall-bounded flow (based on comparison with the model error in the turbulent channel [2]) in the upstream region and then becoming more like the planar jet (see Fig. 1) near and within the separation bubble. After the reattachment point [Fig. 4(d)], there is a superposition of these different qualitative behaviors where the behavior resembles a wall-bounded flow in the near wall region and a free-shear flow in the far wall region. This superposition can be seen most clearly in the peaks in

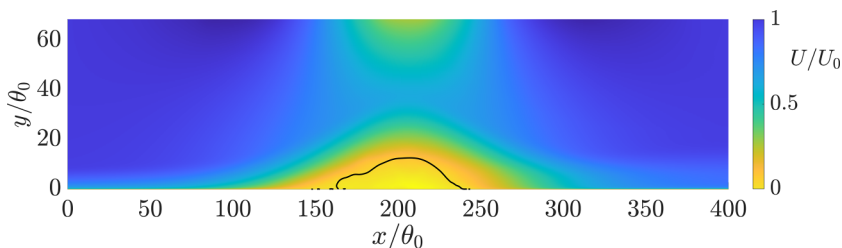


FIG. 3. Mean streamwise velocity in the separation bubble configuration, where — is the streamline that passes through zero streamwise velocity.



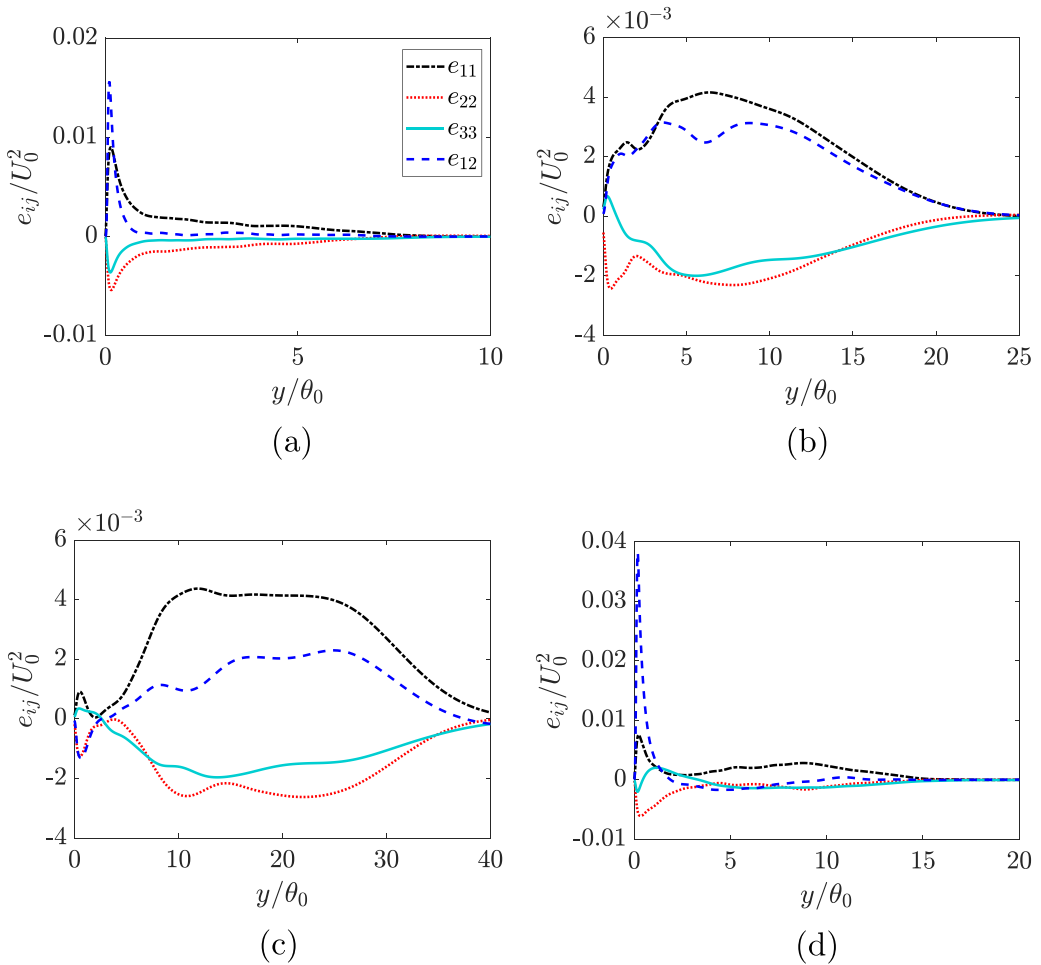


FIG. 4. Comparison of  $e_{ij}$  at different  $x/\theta_0$  locations in the separation bubble configuration. (a)  $x/\theta_0 = 0$ , (b)  $x/\theta_0 = 150$ , (c)  $x/\theta_0 = 200$ , and (d)  $x/\theta_0 = 350$ .

the model error seen at  $y/\theta_0 < 5$ , indicative of the wall-bounded mode, and in the secondary peak in the streamwise model error in Fig. 4(d), indicative of the free-shear mode. As such, two model error modes have been identified: the wall-bounded mode and the free-shear mode.

#### A. Wall-bounded mode

In the wall-bounded mode, the model error behaves as in a canonical wall-bounded flow. Figure 5 shows the model error budgets for the separation bubble at  $x/\theta_0 = 0$  ( $\text{Re}_\tau = 830$ ) compared with those of turbulent channel flow at  $\text{Re}_\tau = 1000$  (data from Lee and Moser [27]). The agreement between these two flows illustrates what is here called the “wall-bounded mode” in the separation bubble: far upstream of the separation point, the flow behaves like a zero pressure gradient boundary layer, so the errors are dominated by the presence of a wall. The sources of these errors are then the same as were found in the channel: production errors arise from misalignment between  $a_{ij}$  and  $S_{ij}$  with contributions from inhomogeneity of the eddy viscosity near the wall to the shear component; dissipation errors arise from the anisotropy of the flow in the near wall region; and the dominant redistribution error found in the shear component arises from misalignment. Additionally,

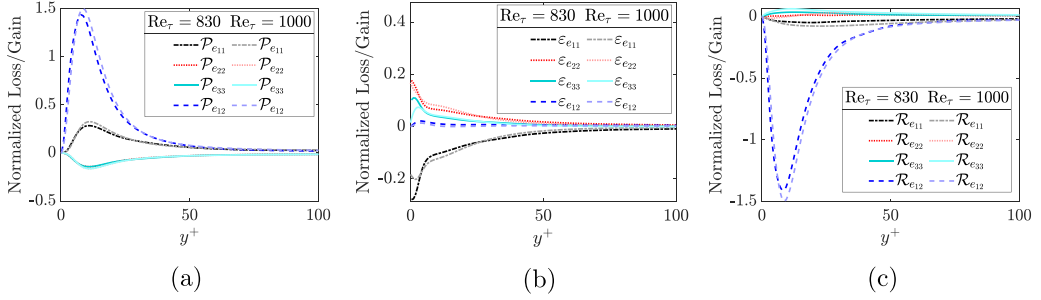


FIG. 5. Comparison of model error budgets in a turbulent channel ( $Re_\tau = 1000$ ) and in the separation bubble configuration ( $Re_\tau = 830$ ) at  $x/\theta_0 = 0$ . (a) Production, (b) Dissipation, and (c) Redistribution.

the magnitude of the normal dissipation errors is found to be equivalent to that of the normal production errors, highlighting the persistence of small-scale anisotropy near the wall.

### B. Free-shear mode

In the free-shear mode, the model error has the qualitative behavior identified in the planar jet (Sec. III). Figure 6 shows the model error budgets at two downstream locations: the first is roughly at the mean separation point  $x/\theta_0 = 150$  and the second is inside the separation bubble at  $x/\theta_0 = 200$ . At these two locations, the effects of separation are clearly displayed, given the departure from the behavior of the model error budgets at  $x/\theta_0 = 0$  in Fig. 5. Primary among these differences is the relative magnitude of the various components. Inside the separation bubble, the components are all also roughly of the same order, highlighting the similarity to the jet flow. This

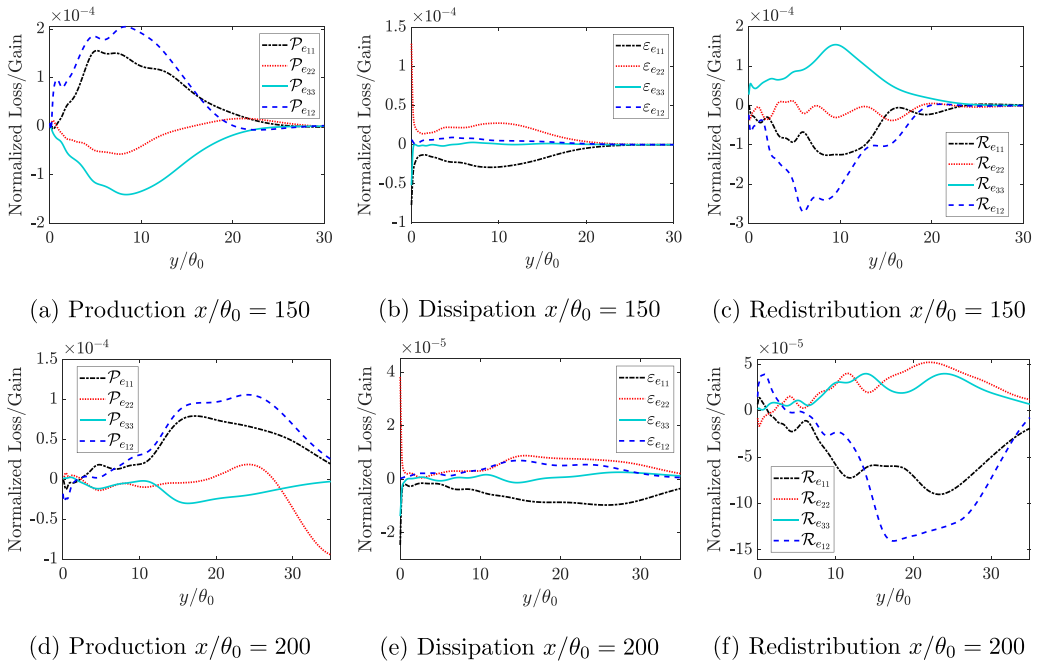


FIG. 6. Budgets of  $e_{ij}$  roughly at (a)–(c) the mean separation point  $x/\theta_0 = 150$  and (d)–(f) within the separation bubble  $x/\theta_0 = 200$ .

is in contrast to the channel, where the shear component is an order of magnitude larger than the normal components in both the model error production and redistribution. Additionally, in the jet, the model error dissipation is an order of magnitude smaller than the production and redistribution, which is also the case away from the wall in the separated region of the separation bubble.

These differences can be further quantified by looking at the terms responsible for the model error budgets at  $x/\theta_0 = 150$  and  $x/\theta_0 = 200$ . The dominant terms in the model error production are largely the same as those found in the turbulent jet in Eqs. (8)–(10), which is in keeping with the sources of model error production in the jet. There are additional misalignment terms that arise from the two-dimensionality of the flow. In the streamwise component, this additional term is minor and is given by

$$-2e_{11} \frac{\partial U_1}{\partial x_1} \quad (14)$$

in the shear component; the additional term is also minor and is given by

$$-e_{11} \frac{\partial U_2}{\partial x_1} \quad (15)$$

and, in the wall-normal component, the additional misalignment terms are given by

$$-2e_{22} \frac{\partial U_2}{\partial x_2} - 2e_{21} \frac{\partial U_2}{\partial x_1} + 2v_T \left( \frac{\partial U_2}{\partial x_1} \frac{\partial U_2}{\partial x_1} + \frac{\partial U_2}{\partial x_2} \frac{\partial U_2}{\partial x_2} \right). \quad (16)$$

These additional misalignment terms differ from the channel as  $\partial U_1/\partial x_1$ ,  $\partial U_2/\partial x_1$ , and  $\partial U_2/\partial x_2$  are zero in unidirectional flows. In the jet, these terms are quite small, so as to be negligible, but this is clearly a feature of the two-dimensionality of the flow. This is exacerbated in the separation bubble as, relative to the planar jet, the properties of the flow are not slowly varying in the streamwise direction, since  $\partial U_1/\partial x_1$ ,  $\partial U_2/\partial x_1$ , and  $\partial U_2/\partial x_2$  become large in this region.

An additional source of model error production is found in the wall-normal component. Towards the outer edge of the separation bubble ( $y/\theta_0 > 20$  at  $x/\theta_0 = 200$ ), the vertical mean pressure gradient becomes important and contributes to the model error production through

$$\frac{2}{\rho} \frac{\partial v_T}{\partial x_2} \frac{\partial P}{\partial x_2}. \quad (17)$$

This arises due to the strong external pressure gradient, reaching a peak at  $x/\theta_0 = 200$ . This differs from both the wall-bounded and free-shear mode errors in that it represents a misalignment error due to rapid changes in the flow, in this case the pressure gradient, not just the strain. Further study of this mode via a flow with a pressure gradient that is not aligned with the direction of the flow, such as a curved channel or free shear flow with an imposed pressure gradient, is necessary in order to isolate other features of its behavior.

In the shear component, the inhomogeneity terms found in Eq. (10) from gradients of the eddy viscosity near the wall are present and behave as they do in the channel very near the wall. These are only found to be significant in the very near wall region ( $y/\theta_0 < 2$ ), and outside of this region the behavior is more similar to that of the planar jet.

The model error redistribution in the separated region comes from a combination of pressure redistribution and misalignment, as found in the planar jet. For the shear component redistribution, this is the same as found in Eq. (13), where misalignment is dominant. For the normal components, the relative contribution of each term changes moving downstream through the separation bubble. At  $x/\theta_0 = 150$ , pressure redistribution and the misalignment term are of the same order of magnitude, but pressure redistribution is larger in the streamwise component and misalignment is larger in the wall-normal component. At  $x/\theta_0 = 200$ , pressure redistribution is larger in both components, and downstream of this the misalignment is slightly larger in both components. In the separation bubble, compared with the planar jet, the properties of the flow are not slowly varying in the streamwise direction, which means that  $\partial U_1/\partial x_1$  and  $\partial U_2/\partial x_2$  become large in this region. Overall, however,

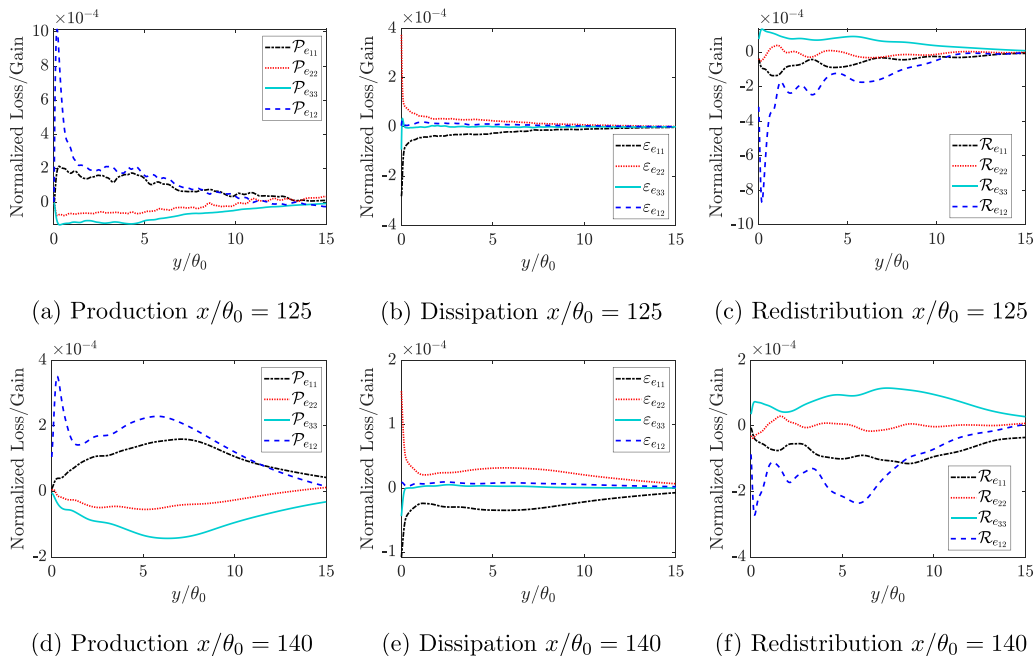


FIG. 7. Budgets of  $e_{ij}$  in the separation bubble configuration at (a)–(c)  $x/\theta_0 = 125$  and (d)–(f)  $x/\theta_0 = 140$ .

the trend of these budgets points to a similarity with the shear flow budgets as opposed to the channel flow budgets.

Interestingly, despite the presence of the wall, there is little influence of the wall on the model error behavior within the separation bubble. This is likely due to the fact that the backflow near the wall is relatively weak, such that the local friction Reynolds numbers (based on the height at which the direction of the flow reverses) at the streamwise locations inside the separation bubble are all less than 40. In a separated flow with a stronger backflow and larger friction Reynolds numbers inside the separation region, it is possible that the model errors present in the wall-bounded mode would be more prevalent within the separation region, at the very least near the wall.

### C. Superposition of model error modes

At intermediate streamwise locations, in between the locations of the distinct wall-bounded mode and free-shear mode, a superposition of the model error modes is observed. Specifically, upstream of the separation point the model error transitions from the wall-bounded mode to the free shear mode, and downstream of the reattachment point the model error transitions from the free-shear mode to the wall-bounded mode. This transition manifests as a superposition of the two modes in which one mode decays as the other grows.

Figure 7 shows the model error budgets at two locations upstream of the separation point in the adverse pressure gradient region at  $x/\theta_0 = 125$  and 140. Near the wall ( $y/\theta_0 < 2$ ), particularly in the shear component, the wall-bounded mode is clear at both locations. This can be seen in the peaks near the wall, particularly in the shear component production and redistribution. It is also clear that the wall-bounded mode decays as the free-shear mode grows moving downstream. The decay of the wall-bounded mode is seen in the decay in the magnitude of the near wall peaks of production and redistribution for all components. In the normal components, the growth of the free-shear mode is evinced in the shift of the peaks of the model error production and redistribution further away from the wall going from  $x/\theta_0 = 125$  to  $x/\theta_0 = 140$ . The normal component model error dissipation

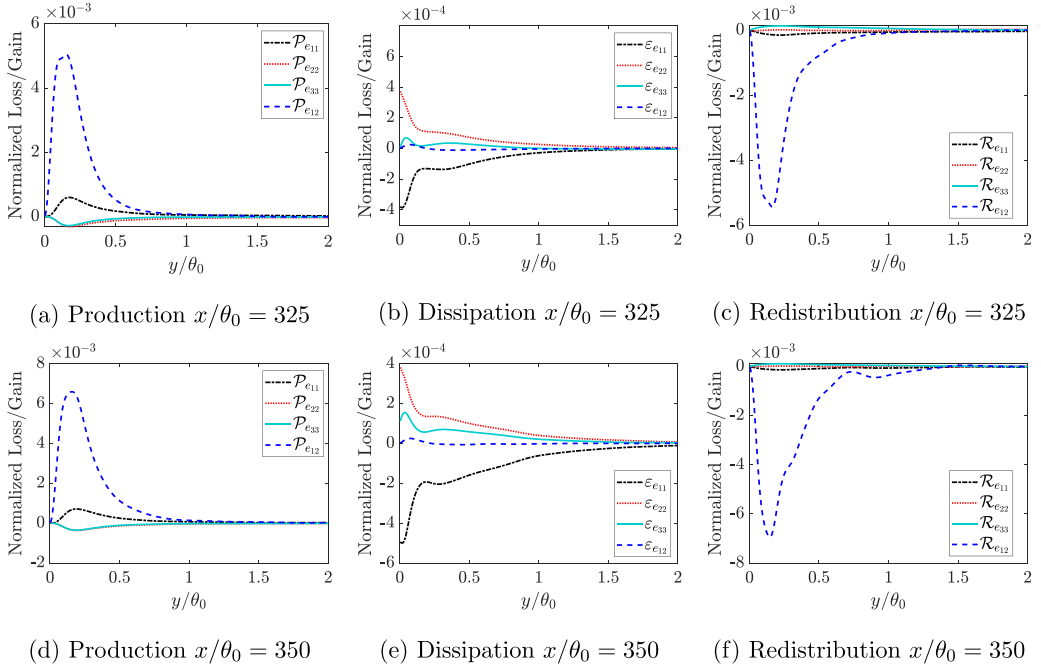


FIG. 8. Budgets of  $e_{ij}$  in the near wall region of the separation bubble configuration at (a)–(c)  $x/\theta_0 = 325$  and at (d)–(f)  $x/\theta_0 = 350$ .

always peaks at the wall, although a secondary peak has formed away from the wall at  $x/\theta_0 = 140$ . In the shear component, particularly in the model error production, the peak in the near wall region decreases in magnitude moving downstream, until it eventually fully decays, as seen at  $x/\theta_0 = 150$  in Fig. 6.

This superposition is also seen downstream of the reattachment point. Figures 8 and 9 show the model error budgets downstream of the reattachment point in the favorable pressure gradient region. Figure 8 shows the wall-bounded mode in the near wall region, and Fig. 9 shows the free-shear mode away from the wall. At these two locations the largest errors are found near the wall and come from the shear component as shown in Figs. 8(a), 8(c), 8(d), and 8(f). In the near wall region, the model error budgets most closely resemble those found in the channel. The dominant terms in the near wall separation bubble budgets are the same as those found at  $x/\theta_0 = 0$ . Note, that there is some contribution from the  $2S_{ij}\overline{Dv_T}/Dt$  terms seen in the model error redistribution in both the near wall and far wall regions [Figs. 8(c), 8(f), 9(c), and 9(f)], which is likely due to a combination of lack of statistical convergence and two-dimensionality effects.

Further away from the wall, the dominant terms are largely the same as those found within the separation bubble. The exception to this is found in the wall-normal and shear components, where inhomogeneity represented by the wall-normal derivative of the eddy viscosity has a dominant role in the model error production and there is a lingering effect of the error mode linked to the mean pressure gradient identified in Sec. IV B. Moving downstream, these two contributions to the model error production decay faster than the contributions linked to the free shear mode, indicating that, as the flow returns to a zero pressure gradient boundary layer, the dominant model error modes are the wall-bounded and free-shear modes. Overall, the qualitative features of the model error budgets away from the wall more closely resemble those of the free-shear mode, specifically the reduced magnitude of the model error dissipation compared with the production and redistribution, as well as the similarity in order of magnitude of each component.

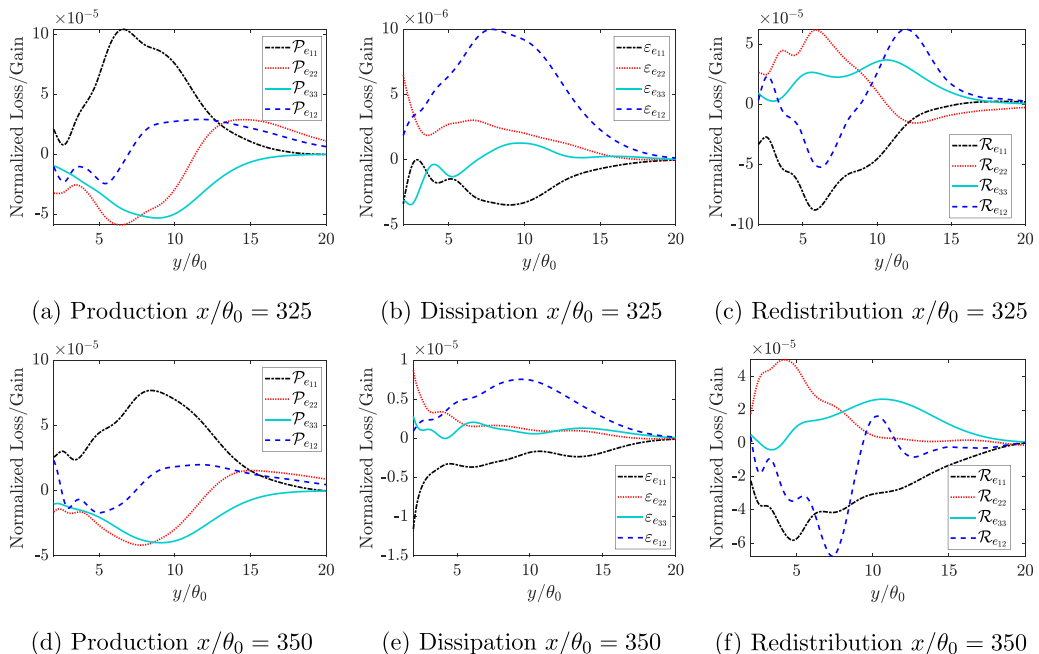


FIG. 9. Budgets of  $e_{ij}$  in the far wall region of the separation bubble configuration at (a)–(c)  $x/\theta_0 = 325$  and (d)–(f)  $x/\theta_0 = 350$ .

The differences between these two locations can be found in the magnitudes of the model error budgets found in the different modes. Looking first at the wall-bounded mode in Fig. 8, an increase in magnitude from  $x/\theta_0 = 325$  to  $x/\theta_0 = 350$  can be clearly seen, particularly in the shear production, streamwise and spanwise dissipation, and the shear redistribution. Similarly, in Fig. 9, a decrease in magnitude from  $x/\theta_0 = 325$  to  $x/\theta_0 = 350$  is observed, especially in the normal components of production, shear and streamwise dissipation, and normal and streamwise redistribution. This perceived exchange of error between the two model error modes illustrates further that these modes are a superposition of canonical flow model errors and that transition from a free-shear flow to a wall-bounded flow can be clearly observed through analysis of the model error.

## V. DISCUSSION

While separated flows pose difficulties for standard RANS models, analysis of the model error for the separation bubble shows that the behavior of the model error is not completely different from canonical flows. In fact, what is perhaps surprising, is the way in which the model error from the two canonical flows (planar jet and channel) can actually be used as building blocks to understand the model error present in the more complex separated flow. These distinct error modes highlight the ways in which certain assumptions contribute more or less to the overall model form error. One particularly notable example of this is the error due to small-scale anisotropy found in the wall-bounded mode, which is not nearly as significant in the free-shear mode. Additionally, these modes provide a useful framework for understanding the error in more complex flows, as evinced by the separation bubble. Even in the region downstream of the reattachment point where both modes are present, the model error can still be understood simply through the superposition of these canonical flow error modes as opposed to a more complicated amalgamation of complex model error modes. Therefore, these simpler flows can be used to understand, locally, the model error in more complex flows.

From a modeling perspective, these model error results further motivate the idea of zonal modeling, which combines models developed for different identifiable zones in the flow associated with different canonical flows [28,29]. While the idea of zonal modeling is not new, the results presented here illustrate that the model errors are largely the result of those associated with simpler canonical flows and that model errors persist as they would in these flows. One of the issues identified with zonal modeling is in the transition regions between different zones in which extra rates of strain are introduced [29]. These extra rates of strain have been identified in the model error budgets presented here, particularly in the error mode identified with the vertical mean pressure gradient, but in this particular case this mode does not seem to overly disrupt the structure of the model error viewed as the superposition of a wall-bounded and free-shear mode. Further study of this effect can be performed through the analysis of a flow with strong pressure gradient effects, such as a curved channel or free-shear flow with an imposed pressure gradient.

With the idea of zonal modeling, models that blend the contributions from the  $k-\varepsilon$  (better suited to free-shear flows) and the  $k-\omega$  (better suited to wall-bounded flows) models, such as the Menter SST model [30], are indicated to be the best approach for handling the error mode switching. The Menter SST model, however, still has the model error associated with the Boussinesq hypothesis (misalignment and small-scale isotropy). One possible avenue to deal with these errors is to use higher-order models that mitigate misalignment and anisotropy errors, such as the SSG/LRR- $\omega$  model [31] that uses the same zonal blending idea from Menter for second-order closure models. The performance of these two models in separated flows, as analyzed in Bai *et al.* [32], illustrates the improvement in the results of the SSG/LRR- $\omega$  model over the Menter SST model due to the increase in physical information. However, an interesting point is revealed in the inability of the higher fidelity model to accurately capture the pressure redistribution term. This indicates the importance of this term, as outlined in the analysis presented here, and also the difficulty presented in trying to accurately model it.

## VI. CONCLUSIONS

In this work, an implied models approach was applied to a turbulent planar jet flow and a turbulent boundary layer over a flat plate with a statistically stationary separation bubble in order to ascertain the sources of model error in the prediction of the anisotropic Reynolds stresses using the  $k-\varepsilon$  and  $k-\omega$  linear eddy viscosity models in these flows and compare them with a previously studied turbulent channel flow. *A priori* analysis was conducted using high fidelity data and the exact transport equations for  $k$ ,  $\varepsilon$ , and  $\omega$ , resulting in a single analysis as the exact formulations of the  $k-\varepsilon$  and  $k-\omega$  models (or other similar models) are equivalent. As stated in Sec. II, this analysis was undertaken in order to study and determine the sources of error in the Boussinesq eddy viscosity model without the obfuscating influence of errors that arise in the *a priori* or *a posteriori* analysis with the model transport equations for  $k$ ,  $\varepsilon$ , and  $\omega$ , which rely on fortuitous error cancellation to be correct [2]. In the turbulent jet flow, the model assumptions contributing to the error were found to be the misalignment of the mean strain rate tensor and the anisotropic Reynolds stress tensor, which gave rise to the production and redistribution errors, and small-scale anisotropy was responsible for the model error dissipation. In comparing the turbulent jet to the turbulent channel, important differences were identified. In the turbulent jet, all four nonzero components of the model error budgets were of roughly the same order of magnitude, while in the channel the shear component errors were an order of magnitude or more larger than the normal component errors. Additionally, in the jet, small-scale anisotropy was found to be far less important given that the dissipation errors were an order of magnitude smaller than the production and redistribution errors, which was not the case in the channel where anisotropy plays a crucial role in the model error dissipation in the near wall region. These differences depict a more complete picture of how the model error behaves in two important canonical flows.

In the separation bubble configuration, the model error was found to have two modes: the wall-bounded mode where sufficiently upstream of the separation bubble the model error budgets

closely resembled those of the turbulent channel and the free-shear mode near and within the separation region where the model error budgets more closely resembled those of the turbulent jet. At intermediate streamwise locations between the two distinct model error modes, such as upstream of the separation point in the adverse pressure gradient region and downstream of the reattachment point in the favorable pressure gradient region, both model error modes were observed. Upstream of the separation point, the wall-bounded mode was found to decay as the free-shear mode grows, and the opposite is found downstream of the reattachment point. These results indicate a complex picture of model error that changes through the flow, but also that calibration of turbulence models against simpler canonical flows may capture the main modes of model failure in more complex flows, such as the separation bubble configuration considered here.

Stated differently, these results suggest that turbulence models applied to more complex flow configurations fail in the same way as in their canonical building blocks, so a model that performs well in all the canonical flows that describe a given complex flow should perform well in the more complex flow. In the absence of such generalizable models, zonal based approaches should similarly be able to perform well in more complex flows with appropriately calibrated blending functions and zonal building blocks.

### ACKNOWLEDGMENTS

K.S.K. gratefully acknowledges the Charlotte Elizabeth Procter Fellowship from Princeton University. The planar jet simulations presented in this article were performed on computational resources supported by the Princeton Institute for Computational Science and Engineering (PICSciE) and the Office of Information Technology's High Performance Computing Center and Visualization Laboratory at Princeton University.

### APPENDIX: IMPLIED MODELS APPROACH FOR NONCONSTANT VISCOSITY

For the separation bubble test case, the viscosity  $\nu$  is taken to be the sum of the subfilter viscosity  $\nu_{SFS}$  and the kinematic viscosity  $\nu_0$ . This modified viscosity is now an instantaneous, spatially varying quantity and is decomposed in the Reynolds-averaging operation, such that  $\nu = \mathcal{V} + \nu'$ , where  $\mathcal{V}$  is the mean total viscosity and  $\nu'$  is the fluctuating total viscosity. The derivation outlined in Klemmer and Mueller [2] is thus altered to include spatial and temporal derivatives of the subfilter viscosity. The modified derivation is shown below.

In this formulation, the anisotropic Reynolds stress transport equation is given by

$$\begin{aligned}
 \frac{\overline{D}a_{ij}}{Dt} = & \underbrace{-\frac{\overline{u'_i u'_k}}{\partial x_k} \frac{\partial U_j}{\partial x_k} - \frac{\overline{u'_j u'_k}}{\partial x_k} \frac{\partial U_i}{\partial x_k} + \frac{2}{3} \frac{\overline{u'_k u'_\ell}}{\partial x_\ell} \delta_{ij}}_I \\
 & - \underbrace{\frac{\partial}{\partial x_k} \left( \frac{\overline{u'_i u'_j u'_k}}{\partial x_k} - \frac{2}{3} \frac{\overline{k u'_k}}{\partial x_k} \delta_{ij} \right)}_{II} - \underbrace{\mathcal{V} \frac{\partial \overline{u'_i u'_j}}{\partial x_k} + \frac{2}{3} \mathcal{V} \frac{\partial k}{\partial x_k} \delta_{ij}}_{III} - \underbrace{\overline{\nu' \frac{\partial u'_i u'_j}{\partial x_k}} + \frac{1}{3} \overline{\nu' \frac{\partial u'_\ell u'_\ell}{\partial x_k}} \delta_{ij}}_{IV} \\
 & - \underbrace{2 \overline{u'_j \nu' S_{ik}} - 2 \overline{u'_i \nu' S_{jk}} + \frac{4}{3} \overline{u'_\ell \nu' S_{\ell k}} \delta_{ij}}_V - \underbrace{\overline{\nu u'_j \frac{\partial u'_k}{\partial x_i}} - \overline{\nu u'_i \frac{\partial u'_k}{\partial x_j}} + \frac{2}{3} \overline{\nu u'_\ell \frac{\partial u'_k}{\partial x_\ell}} \delta_{ij}}_{VI} \\
 & - \underbrace{\overline{\nu' u'_j \frac{\partial u'_k}{\partial x_i}} - \overline{\nu' u'_i \frac{\partial u'_k}{\partial x_j}} + \frac{2}{3} \overline{\nu' u'_\ell \frac{\partial u'_k}{\partial x_\ell}} \delta_{ij}}_{VII} \bigg) - \underbrace{\frac{1}{\rho} \left( u'_i \frac{\partial p'}{\partial x_j} + u'_j \frac{\partial p'}{\partial x_i} \right) + \frac{2}{3\rho} \frac{\partial u'_k p'}{\partial x_k} \delta_{ij}}_{VIII}
 \end{aligned}$$



$$\begin{aligned}
 & \underbrace{-2\nu' \frac{\partial u'_j}{\partial x_k} S_{ik} - 2\nu' \frac{\partial u'_i}{\partial x_k} S_{jk} + \frac{4}{3} \nu' \frac{\partial u'_k}{\partial x_\ell} S_{k\ell} \delta_{ij}}_{\text{IX}} - \underbrace{2\nu' \frac{\partial u'_j}{\partial x_k} s'_{ik} - 2\nu' \frac{\partial u'_i}{\partial x_k} s'_{jk} + \frac{4}{3} \nu' \frac{\partial u'_k}{\partial x_\ell} s'_{k\ell} \delta_{ij}}_{\text{X}} \\
 & \underbrace{-\mathcal{V} \left( \frac{\partial u'_j}{\partial x_k} \frac{\partial u'_k}{\partial x_i} + \frac{\partial u'_i}{\partial x_k} \frac{\partial u'_k}{\partial x_j} - \frac{2}{3} \frac{\partial u'_k}{\partial x_\ell} \frac{\partial u'_\ell}{\partial x_k} \delta_{ij} \right)}_{\text{XI}} - \underbrace{\varepsilon_{ij} + \frac{2}{3} \varepsilon \delta_{ij}}_{\text{XII}}, \tag{A1}
 \end{aligned}$$

where the terms correspond to shear production (I), turbulent transport (II), mean viscous transport (III), fluctuating viscous transport (IV), mixed mean and fluctuating viscous transport terms (V–VII), pressure redistribution (VIII), viscous redistribution (IX), fluctuating dissipation (X), cross dissipation (VI), and dissipation (XII), where  $\varepsilon_{ij} = 2\nu' \frac{\partial u'_i}{\partial x_k} \frac{\partial u'_j}{\partial x_k}$  and  $\varepsilon = \frac{1}{2} \varepsilon_{ii}$ . The transport equation for the mean strain rate  $S_{ij}$  is given by

$$\begin{aligned}
 \frac{\overline{D}S_{ij}}{Dt} = & \underbrace{-\frac{1}{2} \left( \frac{\partial U_k}{\partial x_i} \frac{\partial U_j}{\partial x_k} + \frac{\partial U_k}{\partial x_j} \frac{\partial U_i}{\partial x_k} \right)}_{\text{I}} - \underbrace{\frac{1}{\rho} \frac{\partial^2 P}{\partial x_i \partial x_j}}_{\text{II}} + \underbrace{\frac{\partial}{\partial x_k} \left[ \mathcal{V} \frac{\partial S_{ij}}{\partial x_k} \right]}_{\text{III}} + \underbrace{\mathcal{V} \frac{\partial^2 U_k}{\partial x_i \partial x_j}}_{\text{IV}} \\
 & + \underbrace{\frac{\partial \mathcal{V}}{\partial x_j} S_{ik} + \frac{\partial \mathcal{V}}{\partial x_i} S_{jk}}_{\text{V}} + \underbrace{\frac{\partial}{\partial x_j} \left( \overline{\nu' s'_{ik}} - \frac{1}{2} \overline{u'_i u'_k} \right) + \frac{\partial}{\partial x_i} \left( \overline{\nu' s'_{jk}} - \frac{1}{2} \overline{u'_j u'_k} \right)}_{\text{VI}}, \tag{A2}
 \end{aligned}$$

where (I) can be rewritten as the sum of the inner products of the strain rate tensor with itself and the rotation rate tensor with itself, (II) is the Hessian of the pressure, (III) is viscous transport of the mean strain rate, (IV) and (V) are additional mean viscous transport terms, and (VI) are fluctuating viscous and turbulent transport terms.

For the transport of  $\nu_T$  the exact equations for  $k$ ,  $\varepsilon$ , and  $\omega$  are also modified. The exact transport equation of the turbulent kinetic energy for the case of variable viscosity is given by

$$\begin{aligned}
 \frac{\overline{D}k}{Dt} = & \underbrace{-\overline{u'_i u'_j} \frac{\partial U_i}{\partial x_j}}_{\text{I}} - \underbrace{\frac{\partial}{\partial x_j} \left( \overline{u'_j k} + \frac{1}{\rho} \overline{u'_j p'} - \mathcal{V} \frac{\partial k}{\partial x_j} \right)}_{\text{II}} - \underbrace{\frac{1}{2} \nu' \frac{\partial u'_i u'_i}{\partial x_j}}_{\text{V}} - \underbrace{2\nu' \overline{u'_i S_{ij}}}_{\text{VI}} \\
 & - \underbrace{\mathcal{V} \overline{u'_i \frac{\partial u'_j}{\partial x_i}}}_{\text{VII}} - \underbrace{\mathcal{V} \overline{u'_i \frac{\partial u'_j}{\partial x_i}}}_{\text{VIII}} - \underbrace{2\nu' \overline{u'_i S_{ij}}}_{\text{IX}} - \underbrace{2\nu' \overline{u'_i s'_{ij}}}_{\text{X}} - \underbrace{\mathcal{V} \frac{\partial u'_i}{\partial x_j} \frac{\partial u'_j}{\partial x_i}}_{\text{XI}} - \underbrace{\varepsilon}_{\text{XII}}, \tag{A3}
 \end{aligned}$$

where the terms correspond to shear production (I), turbulent transport (II), pressure transport (III), mean viscous transport (IV), fluctuating viscous transport (V), mixed mean and fluctuating viscous transport (VI)–(VIII), viscous redistribution (IX), fluctuating dissipation (X), cross dissipation (XI), and dissipation (XII). The modified dissipation transport equation, where dissipation is defined using the mean viscosity, is given by

$$\begin{aligned}
 \frac{\overline{D}\varepsilon}{Dt} = & \underbrace{\frac{\partial u'_i}{\partial x_j} \frac{\partial u'_i}{\partial x_j} \overline{D}\mathcal{V}}_{\text{I}} + \underbrace{u'_k \frac{\partial u'_i}{\partial x_j} \frac{\partial u'_i}{\partial x_j} \frac{\partial \mathcal{V}}{\partial x_k}}_{\text{II}} \\
 & - \underbrace{2\nu' \left( \frac{\partial u'_i}{\partial x_k} \frac{\partial u'_j}{\partial x_k} + \frac{\partial u'_k}{\partial x_i} \frac{\partial u'_k}{\partial x_j} \right) \frac{\partial U_i}{\partial x_j}}_{\text{III}} - \underbrace{2\nu' \overline{u'_k \frac{\partial u'_i}{\partial x_j} \frac{\partial^2 U_i}{\partial x_k \partial x_j}}}_{\text{IV}} - \underbrace{2\nu' \frac{\partial u'_i}{\partial x_k} \frac{\partial u'_i}{\partial x_m} \frac{\partial u'_k}{\partial x_m}}_{\text{V}}
 \end{aligned}$$

$$\begin{aligned}
 & + \underbrace{\frac{\partial}{\partial x_j} \left( \mathcal{V} \frac{\partial \varepsilon}{\partial x_j} - \mathcal{V} \frac{\partial \mathcal{V}}{\partial x_j} \frac{\overline{\partial u'_i}}{\partial x_k} \frac{\overline{\partial u'_i}}{\partial x_k} - \mathcal{V} \overline{u'_j} \frac{\overline{\partial u'_i}}{\partial x_m} \frac{\overline{\partial u'_i}}{\partial x_m} - 2 \frac{\mathcal{V}}{\rho} \frac{\overline{\partial p'}}{\partial x_m} \frac{\overline{\partial u'_j}}{\partial x_m} \right)}_{\text{IV}} + \underbrace{\frac{2}{\rho} \frac{\partial \mathcal{V}}{\partial x_i} \frac{\overline{\partial u'_i}}{\partial x_j} \frac{\overline{\partial p'}}{\partial x_j}}_{\text{V}} \\
 & + \underbrace{2\mathcal{V} \frac{\overline{\partial u'_i}}{\partial x_j} \left( 2s'_{ik} \frac{\partial^2 \mathcal{V}}{\partial x_j \partial x_k} + 2 \frac{\overline{\partial s'_{ik}}}{\partial x_j} \frac{\partial \mathcal{V}}{\partial x_k} + \frac{\partial \mathcal{V}}{\partial x_j} \frac{\partial^2 \overline{u'_i}}{\partial x_k \partial x_k} \right) + 2\mathcal{V} \frac{\overline{\partial u'_i}}{\partial x_j} \frac{\partial^2}{\partial x_j \partial x_j \partial x_k} [v'(S_{ik} + s'_{ik})]}_{\text{VI}} \\
 & - \underbrace{4\mathcal{V} \frac{\partial \mathcal{V}}{\partial x_k} \frac{\overline{\partial u'_i}}{\partial x_j} \frac{\partial^2 \overline{u'_i}}{\partial x_j \partial x_k}}_{\text{VII}} - \underbrace{2\mathcal{V}^2 \frac{\partial^2 \overline{u'_i}}{\partial x_k \partial x_m} \frac{\partial^2 \overline{u'_i}}{\partial x_k \partial x_m}}_{\text{VIII}}, \tag{A4}
 \end{aligned}$$

where (I) and (II) are additional mean viscous transport terms, (III) is production, (IV) is transport of dissipation, (V) is an additional mean viscous velocity-pressure gradient term, (VI) are additional mean and fluctuating viscous terms, (VII) is related to the mean viscous dissipation of dissipation, and (VIII) is mean viscous dissipation of dissipation.

Substituting Eqs. (A1)–(A4) into Eq. (2) yields the modified model error transport equation for variable viscosity, incompressible flows:

$$\frac{\overline{De}_{ij}}{Dt} = -e_{ik} \frac{\partial U_j}{\partial x_k} - e_{jk} \frac{\partial U_i}{\partial x_k} + 2v_T \frac{\partial U_i}{\partial x_k} \frac{\partial U_j}{\partial x_k} + \frac{2}{3} (e_{k\ell} - 2v_T S_{k\ell}) \frac{\partial U_k}{\partial x_\ell} \delta_{ij} \tag{A5a}$$

$$+ \frac{\partial v_T}{\partial x_k} \left[ \frac{1}{\rho} \left( \frac{\partial P}{\partial x_i} \delta_{jk} + \frac{\partial P}{\partial x_j} \delta_{ik} \right) + \frac{\partial}{\partial x_j} \left( e_{ik} - 2v_T S_{ik} + \frac{2}{3} k \delta_{ik} - 2\overline{v' s'_{ik}} \right) \right] \tag{A5b}$$

$$+ \frac{\partial}{\partial x_i} \left( e_{jk} - 2v_T S_{jk} + \frac{2}{3} k \delta_{jk} - 2\overline{v' s'_{jk}} \right) \tag{A5c}$$

$$- 2\mathcal{V} \frac{\partial^2 U_k}{\partial x_i \partial x_j} - 2 \frac{\partial \mathcal{V}}{\partial x_j} S_{ik} - 2 \frac{\partial \mathcal{V}}{\partial x_i} S_{jk} \tag{A5d}$$

$$+ \frac{\partial}{\partial x_k} \left[ -\overline{u'_i u'_j u'_k} + \frac{2}{3} \overline{k u'_k} \delta_{ij} - \frac{v_T}{\rho} \left( \frac{\partial P}{\partial x_i} \delta_{jk} + \frac{\partial P}{\partial x_j} \delta_{ik} \right) + \mathcal{V} \frac{\partial e_{ij}}{\partial x_k} \right] \tag{A5e}$$

$$+ v' \frac{\overline{\partial u'_i u'_j}}{\partial x_k} - \frac{1}{3} v' \frac{\overline{\partial u'_\ell u'_\ell}}{\partial x_k} \delta_{ij} + 2\overline{u'_j v' S_{ik}} + 2\overline{u'_i v' S_{jk}} - \frac{4}{3} \overline{u_\ell v' S_{k\ell}} \delta_{ij} \tag{A5f}$$

$$+ \mathcal{V} u'_j \frac{\partial u'_k}{\partial x_i} + \mathcal{V} u'_i \frac{\partial u'_k}{\partial x_j} - \frac{2}{3} \mathcal{V} u'_\ell \frac{\partial u'_k}{\partial x_\ell} \delta_{ij} - 2\mathcal{V} S_{ij} \frac{\partial v_T}{\partial x_k} \tag{A5g}$$

$$+ v' u'_j \frac{\partial u'_k}{\partial x_i} + v' u'_i \frac{\partial u'_k}{\partial x_j} - \frac{2}{3} v' u'_\ell \frac{\partial u'_k}{\partial x_\ell} \delta_{ij} \tag{A5h}$$

$$+ 2v_T \left( \mathcal{V} \frac{\partial^2 U_k}{\partial x_i \partial x_j} + \frac{\partial \mathcal{V}}{\partial x_j} S_{ik} + \frac{\partial \mathcal{V}}{\partial x_i} S_{jk} + \frac{\overline{\partial v' s'_{ik}}}{\partial x_j} + \frac{\overline{\partial v' s'_{jk}}}{\partial x_i} \right) \tag{A5i}$$

$$- v_T \frac{\partial}{\partial x_j} \left( e_{ik} - 2v_T S_{ik} + \frac{2}{3} k \delta_{ik} \right) - v_T \frac{\partial}{\partial x_i} \left( e_{jk} - 2v_T S_{jk} + \frac{2}{3} k \delta_{jk} \right) \tag{A5j}$$

$$- \frac{1}{\rho} \left\langle u'_i \frac{\partial p'}{\partial x_j} + u'_j \frac{\partial p'}{\partial x_i} \right\rangle + \frac{2}{3\rho} \frac{\overline{\partial u'_k p'}}{\partial x_k} \delta_{ij} - 2\mathcal{V} \frac{\partial v_T}{\partial x_k} \frac{\partial S_{ij}}{\partial x_k} - \frac{4}{3} k S_{ij} \tag{A5k}$$

$$+ \frac{4v_T S_{ij}}{k} \left[ -(e_{k\ell} - 2v_T S_{k\ell}) \frac{\partial U_k}{\partial x_\ell} - \frac{\partial}{\partial x_k} \left( \overline{k u'_k} + \frac{1}{\rho} \overline{p' u'_k} - \mathcal{V} \frac{\partial k}{\partial x_k} \right) \right] \tag{A5l}$$

$$- \frac{1}{2} \overline{v' \frac{\partial u'_\ell u'_\ell}{\partial x_k}} - 2 \overline{v' u'_\ell S_{k\ell}} - \overline{\nu u'_\ell \frac{\partial u'_k}{\partial x_\ell}} - \overline{v' u'_\ell \frac{\partial u'_k}{\partial x_\ell}} \quad (\text{A5m})$$

$$- 2 \overline{v' \frac{\partial u'_k}{\partial x_\ell} S_{k\ell}} - 2 \overline{v' \frac{\partial u'_k}{\partial x_\ell} s'_{k\ell}} - \overline{\nu \frac{\partial u'_k}{\partial x_\ell} \frac{\partial u'_\ell}{\partial x_k}} - \varepsilon \quad (\text{A5n})$$

$$- \frac{2\nu_T S_{ij}}{\varepsilon} \left[ \frac{\partial \mathcal{V}}{\partial t} \overline{\frac{\partial u'_k}{\partial x_\ell} \frac{\partial u'_k}{\partial x_\ell}} + \left( U_m \overline{\frac{\partial u'_k}{\partial x_\ell} \frac{\partial u'_k}{\partial x_\ell}} + u'_m \overline{\frac{\partial u'_k}{\partial x_\ell} \frac{\partial u'_k}{\partial x_\ell}} \right) \frac{\partial \mathcal{V}}{\partial x_m} \right] \quad (\text{A5o})$$

$$- 2\mathcal{V} \left( \overline{\frac{\partial u'_k}{\partial x_m} \frac{\partial u'_\ell}{\partial x_m}} + \overline{\frac{\partial u'_m}{\partial x_k} \frac{\partial u'_m}{\partial x_\ell}} \right) \frac{\partial U_k}{\partial x_\ell} - 2\mathcal{V} u'_m \overline{\frac{\partial u'_k}{\partial x_\ell} \frac{\partial^2 U_k}{\partial x_m \partial x_\ell}} \quad (\text{A5p})$$

$$- 2\mathcal{V} \overline{\frac{\partial u'_k}{\partial x_m} \frac{\partial u'_k}{\partial x_n} \frac{\partial u'_m}{\partial x_n}} + \frac{2}{\rho} \frac{\partial \mathcal{V}}{\partial x_k} \overline{\frac{\partial u'_k}{\partial x_\ell} \frac{\partial p'}}{\partial x_\ell} \quad (\text{A5q})$$

$$+ \frac{\partial}{\partial x_\ell} \left( \mathcal{V} \frac{\partial \varepsilon}{\partial x_\ell} - \mathcal{V} \frac{\partial \mathcal{V}}{\partial x_\ell} \overline{\frac{\partial u'_k}{\partial x_m} \frac{\partial u'_k}{\partial x_m}} - \overline{\nu u'_\ell \frac{\partial u'_k}{\partial x_m} \frac{\partial u'_k}{\partial x_m}} - 2 \frac{\mathcal{V}}{\rho} \overline{\frac{\partial p'}{\partial x_m} \frac{\partial u'_\ell}{\partial x_m}} \right) \quad (\text{A5r})$$

$$+ 2\mathcal{V} \overline{\frac{\partial u'_k}{\partial x_\ell} \left( 2s'_{km} \frac{\partial^2 \mathcal{V}}{\partial x_\ell \partial x_m} + 2 \frac{\partial s'_{km}}{\partial x_\ell} \frac{\partial \mathcal{V}}{\partial x_m} + \frac{\partial \mathcal{V}}{\partial x_\ell} \frac{\partial^2 u'_k}{\partial x_m \partial x_m} \right)} \quad (\text{A5s})$$

$$+ 2\mathcal{V} \overline{\frac{\partial u'_k}{\partial x_\ell} \frac{\partial^2}{\partial x_\ell \partial x_\ell \partial x_m} [v'(S_{km} + s'_{km})]} - 4\mathcal{V} \overline{\frac{\partial \mathcal{V}}{\partial x_m} \frac{\partial u'_k}{\partial x_\ell} \frac{\partial^2 u'_k}{\partial x_\ell \partial x_m}} \quad (\text{A5t})$$

$$- 2\mathcal{V}^2 \overline{\frac{\partial^2 u'_k}{\partial x_m \partial x_n} \frac{\partial^2 u'_k}{\partial x_m \partial x_n}} \left] - 2\nu' \overline{\frac{\partial u'_j}{\partial x_k} S_{ik}} - 2\nu' \overline{\frac{\partial u'_i}{\partial x_k} S_{jk}} + \frac{4}{3} \nu' \overline{\frac{\partial u'_k}{\partial x_\ell} S_{k\ell} \delta_{ij}} \quad (\text{A5u})$$

$$- 2\nu' \overline{\frac{\partial u'_j}{\partial x_k} s'_{ik}} - 2\nu' \overline{\frac{\partial u'_i}{\partial x_k} s'_{jk}} + \frac{4}{3} \nu' \overline{\frac{\partial u'_k}{\partial x_\ell} s'_{k\ell} \delta_{ij}} \quad (\text{A5v})$$

$$- \mathcal{V} \left( \overline{\frac{\partial u'_j}{\partial x_k} \frac{\partial u'_k}{\partial x_i}} + \overline{\frac{\partial u'_i}{\partial x_k} \frac{\partial u'_k}{\partial x_j}} - \frac{2}{3} \overline{\frac{\partial u'_k}{\partial x_\ell} \frac{\partial u'_\ell}{\partial x_k} \delta_{ij}} \right) - \varepsilon_{ij} + \frac{2}{3} \varepsilon \delta_{ij}, \quad (\text{A5w})$$

where the terms can be classified as follows: (A5a)–(A5d) are production terms, (A5e)–(A5j) are transport terms, (A5k)–(A5u) are redistribution terms, and (A5v)–(A5w) are dissipation terms.

- 
- [1] D. C. Wilcox, *Turbulence Modeling for CFD* (DCW Industries Inc, 2006).
- [2] K. S. Klemmer and M. E. Mueller, Implied models approach for turbulence model form physics-based uncertainty quantification, *Phys. Rev. Fluids* **6**, 044606 (2021).
- [3] E. Goncalves and R. Houdeville, Reassessment of the wall functions approach for RANS computations, *Aerosp. Sci. Technol.* **5**, 1 (2001).
- [4] F. R. Menter, Two-equation eddy-viscosity turbulence models for engineering applications, *AIAA J.* **32**, 1598 (1994).
- [5] T. Jie and J. Jie, Stress limiter consideration for  $k$ - $\omega$  turbulence models in shock-wave/turbulent boundary-layer interactions in supersonic and hypersonic flows, in *20th AIAA Computational Fluid Dynamics Conference* (2011), p. 3980.
- [6] C. Speziale and S. Thangam, Analysis of an RNG based turbulence model for separated flows, *Int. J. Eng. Sci. (Oxford, UK)* **30**, 1379 (1992).

- [7] H. Lübcke, S. Schmidt, T. Rung, and F. Thiele, Comparison of LES and RANS in bluff-body flows, *J. Wind Eng. Ind. Aerodyn.* **89**, 1471 (2001).
- [8] T. Knopp, T. Alrutz, and D. Schwamborn, A grid and flow adaptive wall-function method for RANS turbulence modelling, *J. Comput. Phys.* **220**, 19 (2006).
- [9] M. L. Shur, P. R. Spalart, M. K. Strelets, and A. K. Travin, A hybrid RANS-LES approach with delayed-DES and wall-modelled LES capabilities, *Int. J. Heat Fluid Flow* **29**, 1638 (2008).
- [10] G. Iaccarino, A. A. Mishra, and S. Ghili, Eigenspace perturbations for uncertainty estimation of single-point turbulence closures, *Phys. Rev. Fluids* **2**, 024605 (2017).
- [11] C. Górlé, S. Zeoli, M. Emory, J. Larsson, and G. Iaccarino, Epistemic uncertainty quantification for Reynolds-averaged Navier-Stokes modeling of separated flows over streamlined surfaces, *Phys. Fluids* **31**, 035101 (2019).
- [12] R. L. Thompson, A. A. Mishra, G. Iaccarino, W. Edeling, and L. Sampaio, Eigenvector perturbation methodology for uncertainty quantification of turbulence models, *Phys. Rev. Fluids* **4**, 044603 (2019).
- [13] K. Stephanopoulos, I. Witte, T. Wray, and R. K. Agarwal, Uncertainty quantification of turbulence model coefficients in OpenFOAM and Fluent for mildly separated flows, in *46th AIAA Fluid Dynamics Conference* (2016), p. 4401.
- [14] M. C. Dunn, B. Shotorban, and A. Frendi, Uncertainty quantification of turbulence model coefficients via latin hypercube sampling method, *J. Fluids Eng.* **133**, 041402 (2011).
- [15] C. Górlé, J. Larsson, M. Emory, and G. Iaccarino, The deviation from parallel shear flow as an indicator of linear eddy-viscosity model inaccuracy, *Phys. Fluids* **26**, 051702 (2014).
- [16] M. Emory, J. Larsson, and G. Iaccarino, Modeling of structural uncertainties in Reynolds-averaged Navier-Stokes closures, *Phys. Fluids* **25**, 110822 (2013).
- [17] O. Desjardins, G. Blanquart, G. Balarac, and H. Pitsch, High order conservative finite difference scheme for variable density low Mach number turbulent flows, *J. Comput. Phys.* **227**, 7125 (2008).
- [18] J. F. MacArt and M. E. Mueller, Semi-implicit iterative methods for low Mach number turbulent reacting flows: Operator splitting versus approximate factorization, *J. Comput. Phys.* **326**, 569 (2016).
- [19] MATLAB, version 7.10.0 (R2021a) (The MathWorks Inc., Natick, Massachusetts, 2021).
- [20] A. A. Townsend, Local isotropy in the turbulent wake of a cylinder, *Aust. J. Sci. Res.* **1**, 161 (1948).
- [21] L. Bradbury, The structure of a self-preserving turbulent plane jet, *J. Fluid Mech.* **23**, 31 (1965).
- [22] J. Rotta, Statistical theory of nonhomogeneous turbulence. Part II, *Eur. Phys. J. A* **131**, 51 (1951).
- [23] M. Takahashi, K. Iwano, Y. Sakai, and Y. Ito, Experimental investigation on destruction of Reynolds stress in a plane jet, *Exp. Fluids* **60**, 46 (2019).
- [24] W. Wu and U. Piomelli, Effects of surface roughness on a separating turbulent boundary layer, *J. Fluid Mech.* **841**, 552 (2018).
- [25] U. Piomelli, A. Rouhi, and B. J. Geurts, A grid-independent length scale for large-eddy simulations, *J. Fluid Mech.* **766**, 499 (2015).
- [26] A. Rouhi, U. Piomelli, and B. J. Geurts, Dynamic subfilter-scale stress model for large-eddy simulations, *Phys. Rev. Fluids* **1**, 044401 (2016).
- [27] M. Lee and R. D. Moser, Direct numerical simulation of turbulent channel flow up to  $Re_\tau \approx 5200$ , *J. Fluid Mech.* **774**, 395 (2015).
- [28] K.-L. Tzuoo, J. H. Ferziger, and S. J. Kline, Zonal Models of Turbulence and Their Application to Free Shear Flows, Tech. Rep. TF-27 (Stanford University, 1986).
- [29] P. Bradshaw, Effects of extra rates of strain - Review, in *Near-Wall Turbulence* (Hemisphere, 1990), pp. 106–122.
- [30] F. R. Menter, Zonal two equation  $k-\omega$  turbulence models for aerodynamic flows, in *Proc. of the 23rd Fluid Dynamics, Plasmadynamics, and Lasers Conference*, AIAA (1993), p. 2906.
- [31] B. Eisfeld and O. Brodersen, Advanced turbulence modelling and stress analysis for the DLR-F6 configuration, in *23rd AIAA Applied Aerodynamics Conference* (2005), p. 4727.
- [32] R. Bai, J. Li, F. Zeng, and C. Yan, Mechanism and performance differences between the SSG/LRR- $\omega$  and SST turbulence models in separated flows, *Aerospace* **9**, 20 (2022).